Development of novel theranostic agents for in vivo amyloid imaging and protective effects on human neuroblastoma cells

Yongliang Li, Longjia Yan, Jing Cai, Wanzheng Zhang, Li Li, Zhiyun Du, Changzhi Dong, B. Meunier, Huixiong Chen

Development of novel theranostic agents for *in vivo* amyloid imaging and protective effects on human neuroblastoma cells

Yongliang Li,[a,⊥] Longjia Yan,[a,⊥] Jing Cai,[c,⊥] Wanzheng Zhang,[a] Li Li,[c] Zhiyun Du,[a] Changzhi Dong,[a,d] Bernard Meunier,[a,e] Huixiong Chen, [a,b,*]

[a]Faculty of Light Industry and Chemical Engineering, Guangdong University of Technology, Guangdong, 510006, China;

[b]CNRS, UMR8601, Laboratoire de Chimie et Biochimie Pharmacologiques et Toxicologiques, CBNIT, Université Paris Descartes, PRES Sorbonne Paris Cité, UFR Biomédicale, 75006 Paris, France;

[c]Imaging Diagnosis and Interventional Center, State Key Laboratory of Oncology in South China, Sun Yat-sen University Cancer Center, Guangzhou, Guangdong 510060, China

[d]Université Paris Diderot, Sorbonne Paris Cité, ITODYS, UMR 7086 CNRS, 75013 Paris, France;

[e]Laboratoire de Chimie de Coordination du CNRS, 205 Route de Narbonne, 31077 Toulouse Cedex, France.

[*]Corresponding author: Huixiong Chen, phone: (+33)142864085, Email: huixiong.chen@parisdescartes.fr

[⊥]They contributed equally to this work

Abstract

Brain amyloid deposits have been identified as the main neuropathological hallmarks of Alzheimer's diseases (AD) and intensive efforts have been devoted to develop aggregation inhibitors preventing the formation of toxic oligomeric Aβ for therapeutic. In addition, evidence indicates that the formation and accumulation of β–amyloid plaques probably precede clinical symptoms by around 20 years and imaging of such plaques would be beneficial for early-stage AD detection. In this study, we investigated phenothiazine-based compounds as novel promising theranostic agents for AD. These multifunctional agents exhibited BBB permeability, low neurotoxicity, good bio-stability as well as strong turn-on fluorescence with a Stokes shift upon binding to Aβ aggregates. They had metal-chelating property which could delay Aβ aggregation and displayed high binding affinity for β–amyloid aggregates. Moreover, they have been simultaneously applied to perform in vivo near-infrared fluorescence imaging of β-amyloid plaques in double transgenic AD mouse model, to prevent self-aggregation of Aβ monomer from forming toxic oligmers and to protect human neuroblastoma SH-SY5Y cells against Aβ-induced toxicity and oxidative stress.

Keywords: Amyloid imaging, Inhibitors, Theranostic agents, Alzheimer's disease

1. Introduction

The misfolding and aggregation of specific proteins in the brain is the main hallmarks of several neurodegenerative diseases [1,2]. In Alzheimer's disease, the two principal aggregating proteins are β-amyloid (Aβ) and tau, which have been considered as potential drug targets up to now. An imbalance between production and clearance, and aggregation of Aβ led to the accumulation of insoluble β-stranded fibrils, which was strongly promoted by the increased concentrations of metal ions such as copper and iron [3]. The primary component of extracellular amyloid deposits is composed of two peptides, $A\beta_{1-40}$ and $A\beta_{1-42}$, which can aggregate into initial protofilaments via self-assembly process followed by insoluble amyloid fibrils through a number of intermediate structural forms including soluble oligomers [4,5]. Recent studies suggest that oligomeric soluble Aβ formes, specifically dimers and trimers are shown to disrupt learning behavior in rats [6] and principally responsible for the pathogenesis of AD, and its levels are more vital in disease progression [7]. Indeed, Aβ oligomers can directly cause neuron death, synaptic dysfunction, a progressive memory loss and a cognitive decline [8–10]. They can also trigger events such as oxidative damage,

inflammation and calcium deregulation [11–13]. which are responsible for AD initiation and progression. Moreover, the soluble Aβ oligomers can result in tau hyperphosphorylation, leading to disruption of the microtubule skeleton and neuritic degeneration [14]. Therefore, small molecule inhibitors of β–amyloid aggregation as a potential therapeutic strategy for AD have attracted the most attention so far [15,16]. On the other hand, the timing of therapeutic intervention of AD is considered a critical issue in the successful development of new drugs, as pathological processes that are still reversible would be targeted [17]. These amyloidogenic deposits precede much earlier than clinical symptoms. Thus, imaging of such β–amyloid aggregates is increasingly recognized as a promising approach to detect the disease at its early onset [18].

Molecular therapeutics combines treatment and diagnosis to monitor response to treatment and improve drug efficacy and safety. They can produce meaningful pharmacokinetic and biodistribution information for the exact molecular target before, during, and after treatment and provide a more specific and effective system for the therapy of disease. Recent advances in optical imaging technologies, which make a significant impact in diagnostic and interventional imaging over the next decade, have promoted the development of fluorescent probes into a fast-developing era [19]. Moreover, modern and efficient optical imaging systems such as fluorescence molecular tomography (FMT) imaging and the hydrid technique known as FMT-CT imaging have allowed to plot the three-dimensional information on the anatomical scans with a high definition and use prior information on the optical properties of tissue to improve both sensitivity and resolution [20,21]. These advanced optical imaging techniques with the utilization of near infrared fluorescent tracers are non-invasive research tools, do not cause radiation damage and offer the potential for significant improvements in image fidelity. Recently, a number of NIR fluorophores have been developed and employed for AD imaging in vivo [22,23]. However, very few of NIR probes used as molecular theranostics have been available and their clinical application remains challenging.

As described previously, phenothiazine derivatives could act both as inhibitors of β-amyloid aggregation and imaging probes for amyloid plaques in Alzheimer's disease [24]. In order to improve ADME properties, in particular aqueous solubility and bioavailability and to increase chelating ability for metal ions of these compounds, we have modified their structure at its periphery by introduction of water solubilizing and/or chelating groups (Scheme 1). Metal ion chelators, such as Clioquinol and its derivative PBT-2 have been tested for AD

treatment in clinical trials, which could efficiently improve cognition in AD patients [25,26]. Herein, we report the synthesis, characterization and biological evaluation of these compounds namely **PHTZs**, as novel theranostic agents for AD.

2. Results and discussion

2.1. Chemistry

The synthetic route to **PHTZs** is proposed in Scheme 1. The rhodanine derivative **1** was prepared by the condensation of 2-(4-oxo-2-thioxothiazolidin-3-yl)acetic acid with (2,2-dimethyl-[1,3]dioxolan-4-yl)-methanol in the presence of DCC and DMAP or with diethyl iminodiacetate and di-tert-butyl iminodiacetate in the presence of HATU and DIEA (Scheme S1). 10-Methyl-10H-phenothiazine-3-carbaldehyde was produced as previously described by reacting phenothiazine with methyl iodide in DMF in the presence of NaH and followed by Vilsmeier-Haack formylation with $POCl_3$ in DMF [24]. The aldehyde obtained was then used to perform a Knoevenagel condensation reaction with the appropriate rhodanine derivative **1** in the presence of piperidine. Finally, **PHTZ-1** and **PHTZ-3b** can be hydrolyzed to give the corresponding compounds **PHTZ-1** and **PHTZ-4**.

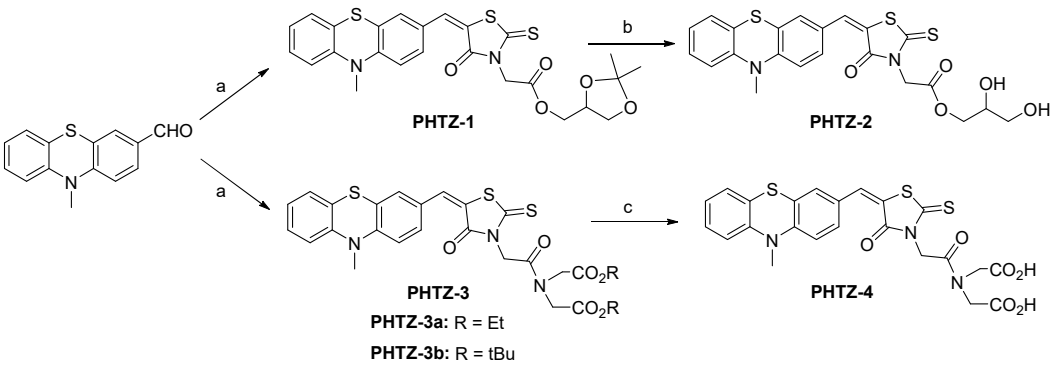

Scheme 1: Reagents and conditions: (a) rhodanine derivative **1**, piperidine, THF; (b) HCl, THF; (c) TFA, DCM.

2.2. Fluorescent properties, metal chelation and in vitro characterizations

First, we evaluated spectroscopic properties of **PHTZs**. As shown in Table 1, **PHTZ-1, PHTZ-2** and **PHTZ-3a** exhibited emission wavelength of 670, 640 and 670 nm in PBS, respectively, which are suitable for NIR probes. Except for **PHTZ-4**, emission wavelength was only 565 nm in PBS. In addition, these agents displayed high sensitivity to the solvent polarity, and the higher fluorescence emission maxima were observed for increasing solvent polarities (Fig. S1), suggesting that they might be very sensitive to the surrounding

environment and show high spatial and temporal resolution. Moreover, the plot of fluorescence intensity versus concentration of these agents showed linear correlation in the range of 0-10 μM with a correlation coefficient of 0.994 (Fig. S2).

Table 1. Fluorescent properties, binding data and calculated log P (clog P) value of **PHTZs**

N°	λ_{abs}[a](nm)	λ_{em1}[b](nm)	λ_{em2}[b](nm)	Φ (%)[c]	fold[d]	K_d (nM)[e]	log P [f]	clog P [f]
PHTZ-1	495	670	615	6.8/0.5	22.0	24.5±2.0	3.65	4.77
PHTZ-2	470	640	615	2.9/0.8	9.5	34.9±3.7	2.29	3.06
PHTZ-3a	490	670	615	4.6/0.5	38.3	46.3± 5.2	3.54	4.50
PHTZ-4	425	565	575	1.2/0.05	2.4	76.5± 7.2	2.34	3.34

[a]Absorbance (λ_{abs}) measured in PBS. [b]Determined in PBS (λ_{em1}) and upon binding with Aβ aggregates (λ_{em2}). [c]Measured in Abeta/PBS, respectively. [d]Fold increase in fluorescence intensity upon binding with Aβ aggregates. [e]K_d value was measured in triplicate with results given as the mean ± SD. [f]The values were calculated using the online ALOGPS 2.1 program.

The ability of **PHTZs** to chelate metal ions of Cu (II) was monitored by UV/Vis titration, as previously reported [27]. Spectral modifications upon addition of aliquots of concentrated aqueous solutions of Cu^{2+} salts were recorded. The evaluation of the affinity of Cu (II) for **PHTZs** is depicted in Figure S3, showing that they have metal-chelating property, particularly for **PHTZ-2 and PHTZ-4**.

Then, we tested the fluorescence response of **PHTZs** toward the synthetic $A\beta_{1-42}$ aggregates in PBS (pH = 7.4). As shown in Figure 1 and Figure S4, the emission intensity increased with the addition of $A\beta_{1-42}$ aggregates, accompanied with Stokes shifts. A remarkable enhancement of fluorescence emission (9.5-38.3 fold) and blue shift (around 10-55 nm) were observed after incubation with $A\beta_{1-42}$ aggregates in PBS, except for **PHTZ-4** which showed only 2.4-fold and a red shift. The binding induced rigid conformation of **PHTZ-4** in PBS probably triggered the modulation of twisted intramolecular charge transfer (ICT) to ICT state conversion and thus led to the red shift of the emission of the probe. Nevertheless, the solvatochromic effect (Fig. S1d) is likely to be the dominant factor for the final bathochromic shift. Conversely, no significant change in fluorescence was observed during incubation with BSA, suggesting that there is a weak interaction between **PHTZs** and BSA (Fig. S5). The binding affinity of **PHTZs** for Aβ aggregates was further assessed through saturation binding assay. The results revealed that they exhibited good affinity for Aβ aggregates with the binding constant (Kd) value of 24.5, 34.9, 46.3 and 76.5 nM, respectively

(Table 1). All these results suggested that **PHTZs** displayed specific turn-on fluorescence upon its interaction with Aβ aggregates.

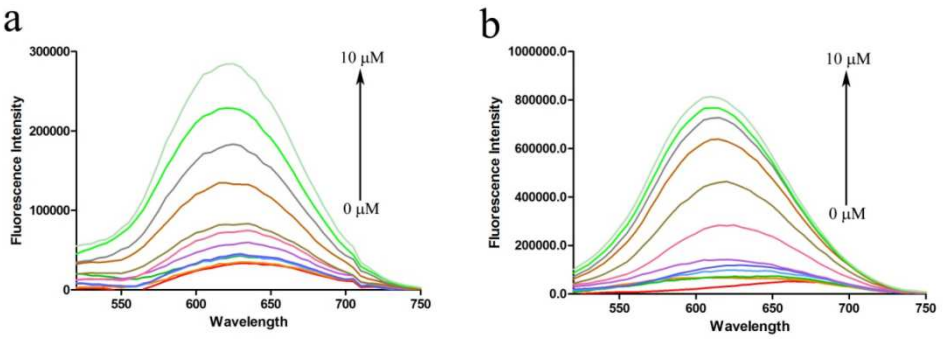

Fig. 1. The fluorescence spectroscopic titration of **PHTZ-1** and **PHTZ-2** (0.2 μM) by stepwise addition of $A\beta_{1\text{-}42}$ aggregates (from 0 μM to 10.0 μM) in PBS (pH = 7.4).

2.3. Photostability, biostability and cytotoxicity

We first investigated the photostability of **PHTZs** and their stability in mice plasma, because it is a prerequisite for showing good in vivo efficacy. The results exhibited that they had good photostability (Figure S6) and were stable with purities higher than 96% after incubation with mice plasma for 30 or 60 min (Figure S7), indicating that **PHTZs** had excellent biostability in plasma and could be developed for in vivo use.

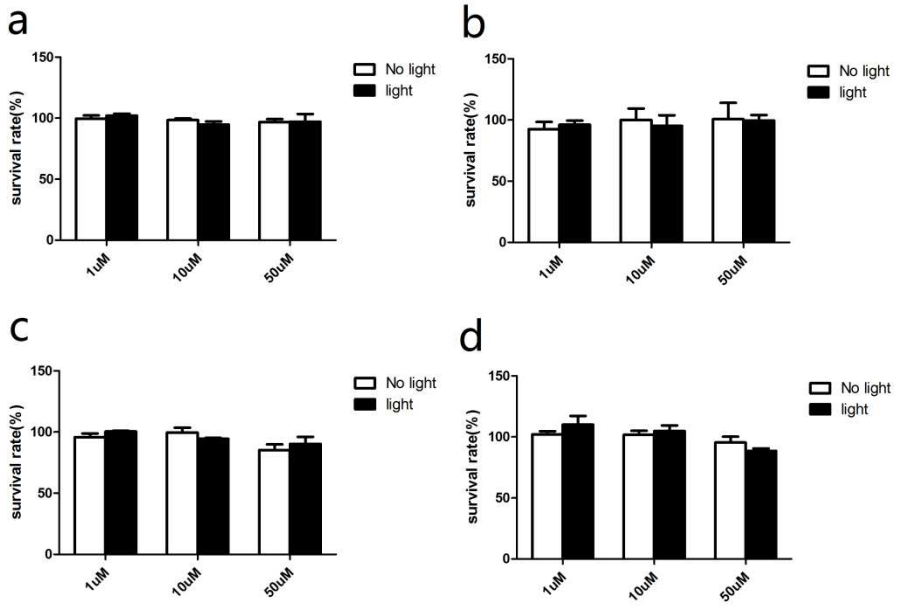

Fig. 2 Cytotoxicity of compounds **PHTZ-1** (a), **PHTZ-2** (b), **PHTZ-3a** (c) and **PHTZ-4** (d) on SH-SY5Y at different concentrations with lighted and without exposure to light.

A cytotoxicity study of **PHTZs** was then carried out by MTT assays with or without exposure to light using a human neuronal cell line (SH-SY5Y) at different concentrations. As shown in Figure 2, **PHTZs** did not show marked toxicity to this human neuronal cell line at 50 μM.

2.4. In vitro fluorescence staining and in vivo imaging

To explore near-infrared fluorescence molecular imaging of selected **PHTZ-1** to β-amyloid plaques in a biologically relevant environment, PHTZ-1 was selected for further study because of the highest binding affinity among these compounds and its good fold increase in fluorescence intensity upon binding with Aβ aggregates. We first conducted a fluorescence staining on the brain tissue from a double Tg mouse overexpressing Aβ (C57BL6, APPswe/PSEN1, 10 months old, male) and an age-matched WT mouse as control. As clearly seen in Figure 3B and 3H, specific staining of Aβ plaques was observed in the cortex region and hippocampus region of the Tg mouse, which was very similar to the observation of staining adjacent slices using Aβ plaque-specific Thioflavin-T dye (ThT) (Figure 3A and 3G). In addition, the fluorescence staining of **PHTZ-1** overlapped well with that of ThT in the cortex region and hippocampus region (Figure 3C and 3I), while no spots were observed on the brain slices from the WT mouse (Figure 3E and 3K) when using **PHTZ-1**. These results clearly indicated that **PHTZ-1** could be used to label β-amyloid plaques.

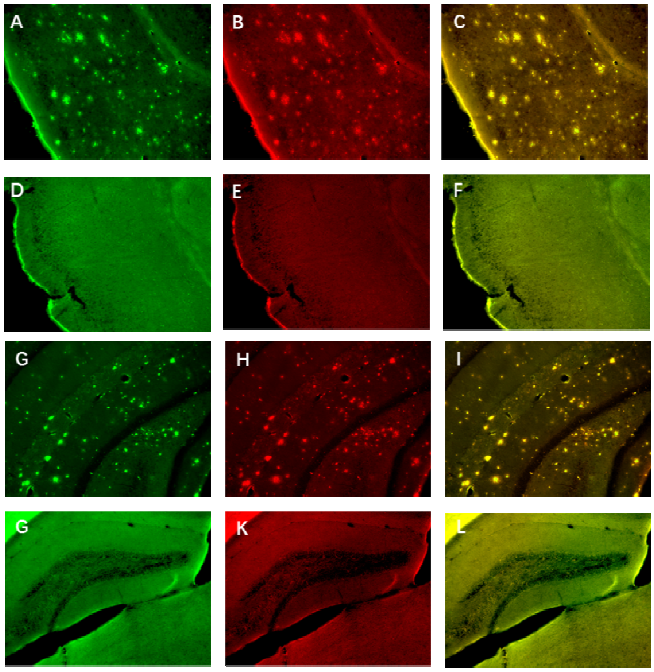

Fig. 3. Fluorescence staining of **PHTZ-1** on brain slices in the cortex region (B) and hippocampus region (H) from a double Tg mouse and WT mice (E and K). Adjacent slices in the cortex region (A) and hippocampus region (G) from Tg mouse were stained with ThT. Brain slices from wild-type control mouse (C57BL/6) was also used in the same conditions with **PHTZ-1** (E and K). Graphical representation of overlap for fluorescence labeling by **PHTZ-1** and ThT (C, F, I and L).

Next, we carried out NIR imaging in vivo by using double transgenic mice (C57BL/6, APP/PS1, 12 months old, male) that exhibited significantly elevated brain amyloid plaques, as compared to age-matched wild mice (C57BL/6, 12 months old, male). As shown in Figure 4, there are considerable differences in fluorescence signals between double transgenic and age-matched wild mice within 5-60 minutes after intravenous administration. Moreover, the fluorescence intensity from the brains of Tg mice diminished at a lower rate than that from the age matched WT, confirming that **PHTZ-1** was capable to detect Aβ plaques *in vivo*.

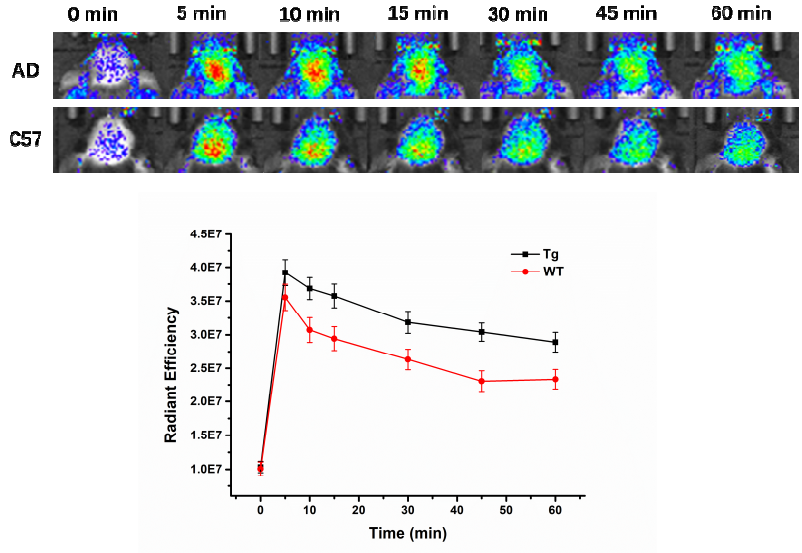

Fig. 4. In vivo imaging study with **PHTZ-1**. (A) Fluorescence images of the same Tg (top row) and WT (bottom row) mouse head at selected time points before or after i.v. injection. (B) Quantitative analysis of fluorescence signals from Tg and control mice after i.v. injection. The signals were significantly higher in 12 month old Tg mice than that in the age matched control mice.

2.5. Inhibitory effect of PHTZs toward Aβ aggregation

To explore the potential therapeutic application of these new theranostic agents, the inhibitory effect of **PHTZ-1** on the $A\beta_{1-42}$ aggregation was first studied in SH-SY5Y cells,

because extracellular soluble Aβ could be uptaken by SH-SY5Y cells and form aggregates in acidic vesicles [28]. Interestingly, this process of intracellular self-aggregation of $A\beta_{1-42}$ could be observed by using fluorescence microscopy. Indeed, as shown in Figure 5, $A\beta_{1-42}$ aggregates could be clearly visualized in SH-SY5Y cells under the fluorescence microscope. On the contrary, the formation of aggregates was notably reduced in the cells treated with **PHTZ-1**. Moreover, **PHTZ-1** has significantly slowed down the aggregation rate of $A\beta_{1-42}$ in a dose-dependent manner, as compared with the control. This result is in accordance with that obtained by using the inhibition assay of $A\beta_{1-42}$ aggregation in vitro, which displayed an IC_{50} value of 0.06 μM (data not shown).

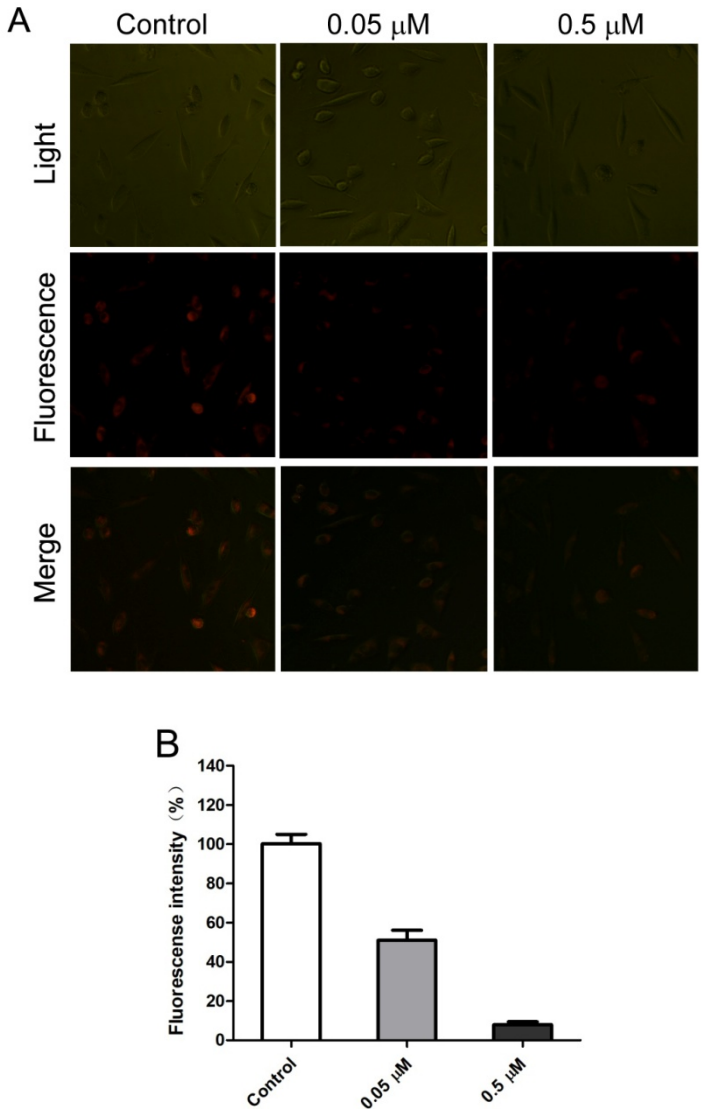

Fig. 5. Inhibition of intracellular self-aggregation of Aβ in SH-SY5Y cells. (A) Cells grown in the presence of Aβ monomer and **PHTZ-1** (0.05 and 0.5 μM) for 2 days, then imaged using fluorescence

microscopy. For control experiment, **PHTZ-1** was added after 2 days without treatment. (B) The histogram represents the fluorescence intensity measured using ImageJ software. Error bars, s.e.m from three independent experiments and four random fields.

2.6. Effect of PHTZs on Aβ$_{1-42}$-induced cell toxicity and ROS production

The neuroprotective effect is one of the important parameters for pharmaceutical potential in AD treatment. Then, we evaluated the protective effects of **PHTZs** against Aβ$_{1-42}$-induced toxicity and ROS production in SHSY5Y cells. Aβ$_{1-42}$-induced toxicity and oxidative stress has been implicated in the progression of Alzheimer's disease [29]. Oxidative stress results in impaired cellular function and the formation of toxic species, which lead to Aβ-induced neurotoxicity and contribute to disease pathogenesis. ROS can be produced by interactions between Redox-active metals such as copper and iron and oxygen species via Fenton/Haber-Weiss reactions and they have been proved to exhibit direct pathological effects leading to various types of neurological disorders [30].

As shown in Figure 6, the cells treated with Aβ$_{1-42}$, (5 μM) alone showed a considerable decrease in the cell viability (about 50%) and a significant increase of ROS level. Conversely, the cells treated with the combination of Aβ$_{1-42}$ and our agents resulted in the increase of cell viability. Meanwhile, the ROS level was also decreased, especially for **PHTZ-2** and **PHTZ-4**, which had a better chelating ability for copper ion (Figure S3). These data indicated that our agents have beneficial neuroprotection to SHSY5Y cells by decreasing Aβ-induced toxicity and attenuating the ROS level.

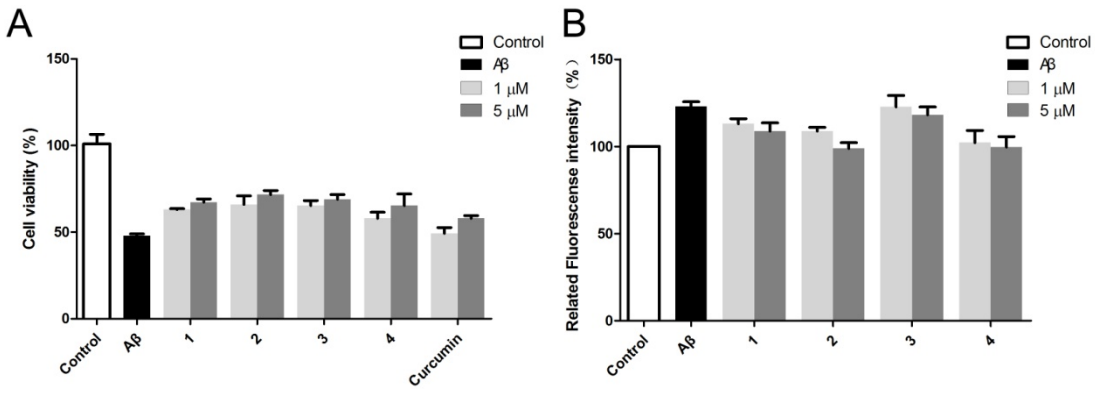

Fig. 6. Cell viability in cultured SH-SY5Y cells (A). Probes attenuated Aβ$_{1-42}$ induced ROS level in SH-SY5Y cells (B). Cells were pretreated with the different concentrations of probes or curcumin.

2.7. ADMET *and Molecular docking studies*

We performed ADMET studies to estimate the solubility, hepatotoxicity, absorption and BBB penetration of these agents. ADMET aqueous solubility logarithmic levels of **PHTZs** were 2, suggesting that these compounds are more soluble than previously described phenothiazine-based compound **4a** [24] (Table S1). ADMET CYP2D6 binding predicts **PHTZ-2**, **PHTZ-3a** and **PHTZ-4** are non-inhibitor of cytochrome P450 enzyme and probably less toxic than **PHTZ-1**. In addition, **PHTZs** were classed as 0 for human intestinal absorption (HIA) and have fallen inside 99% human intestinal absorption confidence ellipsoid (Figure S8), expecting that they possess high human intestinal absorption. Moreover, for ADMET blood brain barrier (BBB), **PHTZ-1** and **PHTZ-2** were classed as 1 and 2 and have fallen inside 99% BBB confidence ellipsoid (Figure S6), showing a good BBB penetration. Except for **PHTZ-3a** and **PHTZ-4**, they have fallen outside 99% BBB ellipse and can be undefined. Furthermore, the calculated log P values of **PHTZs** were 3.65, 2.29, 3.54 and 2.34, respectively (Table 1), suggesting its great potential in BBB penetration.

To gain more details on the interactions of these agents with β–amyloid fibrils, molecular docking studies were performed to predict the plausible interactions between the probe and Aβ fibrils. In this study, two major binding sites at the grooves on the KLVFFA fibril surface were identified as the binding site of "IMPY" formed by the nonpolar residues Val18 and Phe20 running longitudinally to the long axis of the β-sheet and "non-IMPY" site, a wider channel formed by LYS16 and VAL18 [31]. The primary backbones of our agents are very similar, with the difference between them being the structural alterations at its periphery. These agents preferentially bound to the "IMPY site" and were partially buried into "non-IMPY sites" (Figure S9). The formation of one salt bridge was observed between one side of **PHTZ-4** and the Lys16 residue (Figure S10), which resulted in the phenothiazine cycle being more flexible at the grooves of Aβ fibril surface and might lead to not high enhancement of fluorescence intensity upon binding to Aβ aggregates. Among these agents, **PHTZ-1** had the highest affinity of 24.5 nM, which were higher than those of **PHTZ-2** (Kd = 34.9 nM), **PHTZ-3a** (Kd = 46.3 nM) and **PHTZ-4** (Kd = 76.5 ± 7.2 nM). These results accord well with the binding energy of **PHTZ-1** (-9.31 Kcal/mol), **PHTZ-2** (-8.86 Kcal/mol) and **PHTZ-3a** (-8.04 Kcal/mol) with Aβ fibrils, except for **PHTZ-4** (-10.34 Kcal/mol). The discrepancy between the binding affinity and the calculated binding energy for **PHTZ-4** is probably due to our docking simulation being performed in a vacuum without considering the solvation effect. Often, in aqueous solution, solvation effects strongly affect the thermodynamic profile of a

binding event, and thus neglecting these effects may cause substantial errors in the binding energy predictions [32].

3. Conclusion

In the last decade a remarkable progress has been made in the basic research in AD. However, there is still a very heated debate about the potential deficiencies in our understanding of AD physiopathology, lack of validated biomarkers for early-stage diagnosis of AD, choice of therapeutic targets and design of disease-modifying drug for clinical trials. This might explain the failure in the current therapeutic strategies. We have developed several novel theranostic agents. These multifunctional agents displayed BBB permeability, low neurotoxicity, good bio-stability, strong fluorescence enhancement upon interaction with Aβ aggregates accompanied by a blueshift as well as good affinity to Aβ plaques in fluorescent staining of brain sections from double transgenic AD mouse model (APP/PS1). Compared with previously reported theranostic agents such as **4a**, these compounds displayed improved water solubility and higher increase in fluorescence intensity after binding to Aβ aggregates. Moreover, they have been simultaneously applied to perform NIR in vivo imaging of β-amyloid plaques in APP/PS1 mice, to prevent self-aggregation of Aβ monomer in human neuroblastoma cells (SH-SY5Y) and to play neuroprotective effects induced by $A\beta_{1-42}$ in SH-SY5Y cells. Furthermore, **PHTZ-1** exhibited more potent inhibitory activity against $A\beta_{1-42}$ aggregation than our previously reported theranostic agents. Therefore, these novel agents may represent a promising starting point to develop more potent theranostic agents for a possible application of AD treatment.

4. Experimental section

4.1. Chemistry

All reagents and materials were purchased and used without further purification. Analytical thin-layer chromatography was performed on precoated 250 μm layer thickness silica gel 60 F254 plates. Column chromatography was performed using silica gel 300-400 mesh. Melting points were determined on a Kofler apparatus as uncorrected values. ^{1}H NMR and ^{13}C NMR spectra were measured on 400 MHz spectrometer in $CDCl_3$ or DMSO-d6 relative to TMS as internal standard. MS (ESI) was determined by using a QTRAP spectrometer with ion source. Fluorescence and ultraviolet−visible spectra were measured using a spectrofluorophotometer (RF-5301PC, Shimadzu, Japan).

*4.1.1. (4-Oxo-2-thioxo-thiazolidin-3-yl)-acetic acid 2,2-dimethyl-[1,3]dioxolan-4-ylmethyl ester (**1a**).*

To a solution of the (2,2-dimethyl-[1,3]dioxolan-4-yl)-methanol (2.0 mmol, 1 equiv), (4-oxo-2-thioxo-thiazolidin-3-yl)-acetic acid (2.0 mmol, 1 equiv) in 5 mL DCM and DMAP (0.01 mmol, 0.005 equiv) was added at 0°C. Finally, DCC (2.0 mmol, 1 equiv) in 5 mL DCM was added dropwise and the reaction mixture was stirred at at 0°C for 6 hours. The reaction was diluted with 10 mL of DCM and the formed solid was filtered off. The filtrate was dried over anhydrous Na_2SO_4 and the solvents were removed under reduced pressure. The residue was purified by flash chromatography (n-Hexane : EtOAc = 5:1) to give the product as a yellow oil (451 mg, 74%). ^{1}H NMR (400 MHz, $CDCl_3$) δ 4.77 (q, *J* = 16.8 Hz, 2H), 4.34 – 4.23 (m, 2H), 4.17 (dd, *J* = 11.2, 5.6 Hz, 1H), 4.11 – 4.04 (m, 3H), 3.75 (dd, *J* = 8.4, 5.6 Hz, 1H), 1.61 (s, 1H), 1.44 (s, 3H), 1.36 (s, 3H).

*4.1.2. General procedure for the synthesis of **1b-c***

To a solution of the (4-oxo-2-thioxo-thiazolidin-3-yl)-acetic acid (2.0 mmol, 1 equiv), (ethoxycarbonylmethyl-amino)-acetic acid ethyl ester (3.0 mmol, 1.5 equiv) in 6 mL DMF and HATU (3.0 mmol, 1.5 equiv), DIEA (3.0 mmol, 1.5 equiv) was added at 0°C. The reaction mixture was stirred at at room temperature for 12 hours. The mixture was diluted in DCM and washed with brine in three times. The organic phase was dried over $MgSO_4$, filtered and concentrated in vacuum. The crude product was purified by by flash chromatography (n-Hexane : EtOAc = 5:1) to give the title products.

*4.1.2.1. {Ethoxycarbonylmethyl-[2-(4-oxo-2-thioxo-thiazolidin-3-yl)-acetyl]-amino}-acetic acid ethyl ester (**1b**).* Yellow oil. Yield 56%. ^{1}H NMR (400 MHz, $CDCl_3$) δ 4.84 (s, 2H), 4.32 – 4.23 (m, 4H), 4.21 – 4.15 (m, 4H), 4.07 (s, 2H), 1.33 (t, *J* = 7.2 Hz, 3H), 1.26 (t, *J* = 7.2 Hz, 3H).

*4.1.2.2.{tert-Butoxycarbonylmethyl-[2-(4-oxo-2-thioxo-thiazolidin-3-yl)-acetyl]-amino}acetic acid tert-butyl ester (**1c**).* Yellow oil. Yield 48%. ^{1}H NMR (400 MHz, $CDCl_3$) δ 4.81 (s, 2H), 4.10 (s, 2H), 4.08 – 4.07 (m, 4H), 1.52 (s, 9H), 1.45 (s, 9H).

*4.1.3. General procedure for the synthesis of compounds **PHTZ-1** and **PHTZ-3***

To a round bottom flask containing a solution of 10-Methyl-10H-phenothiazine-3-carbaldehyde (0.41 mmol, 1 eq) and compound **1** (0.46 mmol, 1.1 eq) in 5 mL of THF was added piperidine (0.041 mmol, 0.1 eq) and the mixture was heated at 50 °C for 3 hours. The crude mixture was concentrated under reduced pressure and purified by flash chromatography to give the title product

*4.1.3.1. [5-(10-Methyl-10H-phenothiazin-3-ylmethylene)-4-oxo-2-thioxo-thiazolidin-3-yl] acetic acid 2,2-dimethyl-[1,3]dioxolan-4-ylmethyl ester (**PHTZ-1**).* Red solid. Yield 75%. mp: 82 °C. ^{1}H NMR (400 MHz, $CDCl_3$) δ 7.67 (s, 1H), 7.34 (dd, *J* = 8.4, 2.0 Hz, 1H), 7.26 (d, *J* =

2.0 Hz, 1H), 7.22 (t, *J* = 7.6 Hz, 1H), 7.16 (dd, *J* = 7.6, 1.2 Hz, 1H), 7.01 (t, *J* = 7.2 Hz, 1H), 6.87 (dd, *J* = 8.4, 3.6 Hz, 2H), 4.92 (d, *J* = 2.8 Hz, 2H), 4.35 (dt, *J* = 11.2, 5.6 Hz, 1H), 4.30 – 4.20 (m, 2H), 4.09 (dd, *J* = 8.4, 6.4 Hz, 1H), 3.77 (dd, *J* = 8.4, 6.4 Hz, 1H), 3.45 (s, 3H), 1.45 (s, 3H), 1.38 (s, 3H). ^{13}C NMR (400 MHz, $CDCl_3$) δ 192.6, 167.1, 165.8, 148.2, 144.1, 133.3, 131.2, 128.9, 127.8, 127.4, 127.3, 124.6, 123.6, 122.3, 119.6, 114.7, 114.4, 109.9, 73.2, 66.2, 65.8, 44.7, 35.7, 26.7, 25.3. ESI-MS m/z: 529.2 $[M + H]^+$. Anal. Calcd for $C_{25}H_{24}N_2O_5S_3$: C, 56.80; H, 4.58; N, 5.30. Found: C, 56.95; H, 4.55; N, 5.28.

*4.1.3.2. (Ethoxycarbonylmethyl-{2-[5-(10-methyl-10H-phenothiazin-3-ylmethylene)-4-oxo-2-thioxo-thiazolidin-3-yl]-acetyl}-amino)-acetic acid ethyl ester (**PHTZ-3a**).* Red solid. Yield 58%. mp: 152 °C. ^{1}H NMR (400 MHz, $CDCl_3$) δ 7.63 (s, 1H), 7.30 (dd, *J* = 8.4, 2.0 Hz, 1H), 7.23 – 7.17 (m, 2H), 7.13 (dd, *J* = 7.6, 1.2 Hz, 1H), 6.98 (t, *J* = 7.2 Hz, 1H), 6.86 – 6.82 (m, 2H), 4.98 (s, 2H), 4.31 – 4.27 (m, 4H), 4.23 – 4.15 (m, 4H), 3.42 (s, 3H), 1.35 (t, *J* = 7.2 Hz, 3H), 1.26 (t, *J* = 7.2 Hz, 3H). ^{13}C NMR (100 MHz, $CDCl_3$) δ 192.9, 168.6, 168.2, 167.2, 165.5, 148.0, 144.2, 132.9, 131.0, 128.9, 127.8, 127.5, 127.3, 124.4, 123.5, 122.3, 119.9, 114.6, 114.3, 62.2, 61.5, 50.0, 48.6, 44.6, 35.6, 14.2, 14.1. ESI-MS m/z: 586.1 $[M + H]^+$. Anal. Calcd for $C_{27}H_{27}N_3O_6S_3$: C, 55.37; H, 4.65; N, 7.17. Found: C, 55.20; H, 4.67; N, 7.21.

*4.1.3.3. (tert-Butoxycarbonylmethyl-{2-[5-(10-methyl-10H-phenothiazin-3-ylmethylene)-4-oxo-2-thioxo-thiazolidin-3-yl]-acetyl}-amino)acetic acid tert-butyl ester (**PHTZ-3b**).* Red solid. Yield 62%. mp: 157 °C. ^{1}H NMR (400 MHz, $CDCl_3$) δ 7.62 (s, 1H), 7.30 (dd, *J* = 8.4, 2.0 Hz, 1H), 7.23 – 7.16 (m, 2H), 7.13 (dd, *J* = 7.6, 1.2 Hz, 1H), 6.98 (t, *J* = 7.6 Hz, 1H), 6.86 – 6.81 (m, 2H), 4.94 (s, 2H), 4.13 (s, 2H), 4.10 (s, 2H), 3.41 (s, 3H), 1.54 (s, 9H), 1.45 (s, 9H). ESI-MS m/z: 642.1 $[M + H]^+$.

*4.1.4. [5-(10-Methyl-10H-phenothiazin-3-ylmethylene)-4-oxo-2-thioxo-thiazolidin-3-yl]acetic acid 2,3-dihydroxy-propyl ester (**PHTZ-2**).*

A solution of **PHTZ-1** (0.25 mmol, 1 eq) in 4 mL of THF with the solution of HCl/EtOAc (1 mmol, 4 eq) was stirred at room temperature for 3 hours. The crude mixture was concentrated under reduced pressure and purified by flash chromatography to give the product as a red solid (102 mg, 84%). mp: 85 °C. ^{1}H NMR (400 MHz, $CDCl_3$) δ 7.49 (d, *J* = 11.6 Hz, 1H), 7.35 – 7.31 (m, 2H), 7.24 – 7.15 (m, 2H), 7.00 (dd, *J* = 11.2, 4.0 Hz, 2H), 6.87 – 6.80 (m, 2H), 6.66 – 6.59 (m, 1H), 4.89 (d, *J* = 3.2 Hz, 2H), 4.34 (dt, *J* = 11.2, 5.6 Hz, 1H), 4.29 – 4.20 (m, 2H), 4.09 (dd, *J* = 8.4, 6.4 Hz, 1H), 3.77 (dd, *J* = 8.4, 5.6 Hz, 1H), 3.43 (s, 3H), 1.45 (s, 3H), 1.39 (s, 3H). ^{13}C NMR (100 MHz, DMSO) δ 191.9, 166.2, 165.9, 147.79, 144.6, 144.3, 134.0, 129.9, 128.2, 127.7, 127.3, 125.9, 124.2, 123.2, 122.7, 122.5, 120.9,

114.5, 114.2, 109.9, 73.2, 66.3, 65.7, 44.7, 35.6, 26.7, 25.3. ESI-MS m/z: 489.1 $[M + H]^+$. Anal. Calcd for $C_{22}H_{20}N_2O_5S_3$: C, 54.08; H, 4.13; N, 5.73. Found: C, 54.29; H, 4.11; N, 5.70.

*4.1.5. (Carboxymethyl-{2-[5-(10-methyl-10H-phenothiazin-3-ylmethylene)-4-oxo-2-thioxo-thiazolidin-3-yl]acetyl}-amino)-acetic acid (**PHTZ-4**).*

To a round bottom flask containing a solution of compound **PHTZ-3b** (0.4 mmol, 1 eq) in 2 mL of DCM was added 1 mL of TFA and the mixture was stirred at room temperature for 24 hours. The mixture was filtered and the crude product washed by ether to give the compond as a red solid (106 mg, 50%). mp: 258 °C. ^{1}H NMR (400 MHz, DMSO) δ 12.90 (br, 2H), 7.74 (s, 1H), 7.50 (dd, *J* = 8.4, 2.0 Hz, 1H), 7.43 (d, *J* = 2.0 Hz, 1H), 7.27 – 7.23 (m, 1H), 7.19 (dd, *J* = 7.6, 1.2 Hz, 1H), 7.11 (d, *J* = 8.8 Hz, 1H), 7.05 – 6.99 (m, 2H), 4.94 (s, 2H), 4.34 (s, 2H), 4.00 (s, 2H), 3.39 (s, 3H). ^{13}C NMR (100 MHz, DMSO) δ 193.2, 170.8, 170.6, 166.9, 165.79, 148.1, 144.3, 133.2, 131.4, 129.6, 128.6, 127.6, 127.4, 123.9, 123.4, 121.5, 119.5, 115.8, 115.7, 49.9, 49.1, 45.5, 36.0. ESI-MS m/z: 530.1 $[M + H]^+$. Anal. Calcd for $C_{23}H_{19}N_3O_6S_3$: C, 52.16; H, 3.62; N, 7.93. Found: C, 52.37; H, 3.60; N, 7.90.

4.2. Evaluation of Cu^{II} to PHTZ affinity

The affinity of probes for Cu (II) was measured by an Ultraviolet visible spectrophotometer. In brief, to a solution of 20 μM of **PHTZs** in water, the solution of $CuSO_4$ was added (0 to 1000 μM), and total variation of volume in the cuvette was below 2% upon addition of 1000 μM metal. UV/Vis spectrum was recorded after each addition of $CuSO_4$. Results were obtained in triplicate.

4.3. Biological assays

Monomeric $A\beta_{1-42}$ was purchased from GL Biochem. Transgenic mice (APPswe/PSEN1dE9, 12 months old, male) and male C57BL/6 counterparts were provided from GDMLAC (certification number: 44007200000555). All animal test procedures were approved by Sun Yat-sen university animal ethical experimentation Committee.

4.3.1. In vitro plasma stability of PHTZs

The *in vitro* stability of **PHTZs** was studied in rat plasma. To 315 μL of rat plasma from normal SD rat (7 weeks, male) or PBS (as a standard sample) was added 35 μL of **PHTZs** in ethanol (50 μM). The mixture was incubated at 37 °C for 30 or 60 min, treated with 350 μL of CH_3CN and separated by centrifugation at 40000 rpm for 5 min. The supernatant were treated by the same method once again and analyzed by HPLC using a C_{18}

column (4.6 mm × 250 mm) and CH_3CN/H_2O (85:15%) with a flow rate of 1 mL/min at 30 ℃.

4.3.2. MTT assay

Cell viability was determined by a quantitative colorimetric assay using MTT. SH-SY5Y cells were seeded at 5000 cells per well in 96-well plates and incubated overnight. Then the cells were treated for 24 h with **PHTZs** at different concentrations or treated with 5 μM of $A\beta_{1-42}$ monomer and **PHTZs** (1 μM or 5 μM) to evaluate their effect on cell viability in SH-SY5Y. After treatment, MTT solution (5 mg/mL) was added, and the cells were incubated for another 4 h. The absorbance of each well was measured at 570 nm.

4.3.3. In vitro fluorescence staining in brain tissue

Frozen section of brain tissue from double transgenic mice (C57BL/6, APP/PS1, 10 months old, male) and age-matched wild mice (C57BL/6, 10 months old, male) were used for in vitro fluorescent staining. The brain sections were washed in PBS to remove OCT. Next, they were incubated with a 10% ethanol solution (concentration is 1 μM) of **PHTZ-1** or ThT for 5 min at room temperature, and then washed by twice with ethanol and PBS (0.1 M, pH = 7.4) for 10 min. Finally, fluorescent observation was performed by using a fluorescence microscope (Olympus BX63) equipped with GFP and Cy5 filter sets.

4.3.4. In vivo imaging

Double transgenic mice (C57BL/6, APP/PS1, 12 months old, male) and age-matched wild mice (C57BL/6, 12 months old, male) as control were shaved before NIR imaging. The mice were injected with 50 μl of **PHTZ-1** (4 mg/kg) in 20% DMSO and 80% propylene glycol via the tail vein and kept under anesthesia with 2.5% isoflurane gas in an oxygen flow. Fluorescence signals from the brain were recorded at different time points and a filter set (ex. at 500 and em. at 680 nm) was used. The optical images were obtained with an exposure time of 1s. Imaging data were analyzed by Living Image software and the ROI was drawn around the brain region.

4.3.5. Fluorescence staining of Aβ aggregation inhibition

β amyloid peptide aggregation in SH-SY5Y cells was observed by fluorescence microscope (Olympus IX71 inverted fluorescence microscope). Briefly, SH-SY5Y cells were seeded at 2000 cells in 96-well plates. $A\beta_{1-42}$ monomer (0.25 μM) alone or in combination

with **PHTZ-1** (0.05 μM or 0.5 μM) were added and incubated at 37 °C and 5% CO_2 for 48 h. Then, the fluorescence intensity was measured by the average pixel intensity of four random fields using the program ImageJ.

4.3.6. ROS measurement

Intracellular production of ROS in SH-SY5Y cells following $A\beta_{1-42}$ and **PHTZ-1** treatment were determined by Reactive Oxygen Species Assay Kit (Beyotime, China). Briefly, cells were plated at 5000 cells per well in 96-well plates and incubated overnight. After 12h, the culture medium was replaced with Aβ (2 μM, final concentration) alone or in combination with **PHTZ-1** (1 μM and 5 μM), incubating in an incubator at 37 ℃ under a 5% CO_2 atmosphere for 24 h. 10 μM DCFH-DA was added, incubated at 37 ℃ for 30 min and washed twice with culture medium without FBS. The fluorescence intensity of cells was measured by using a microplate reader with excitation/emission at 488/525 nm.

4.3.7. Statistical Analysis

All of the data were analyzed by using the InStat software program (GraphPad Software, San Diego, CA) and student's t test was used. All values are described as mean ± SD and $p \leq 0.05$ was considered statistically significant.

4.4. ADMET and docking study

Computer aided ADME studies have been done by using CHARMM force field (Discovery Studio 2.5 software, Accerlrys, Inc., San Diego, Calif.). Docking procedures were performed using Autodock 4.2 software on Aβ fibril structures from RCSB protein Data Bank (PDB ID: 2LMO) according to the Lamarckian genetic algorithm method. Molecular building and energy minimizing were carried out with Sketch and Minimized modular in Sybyl 6.0 software (Tripos, USA), according to a Tripos force field [33] and Gasteiger-Marsili charges theory [34,35]. The rigid protein was used as the macromolecule receptor and our agents as a flexible ligands with all torsions defined to be rotatable. The segment of 16-KLVFFA-21 from the Aβ fibrils was used as the binding site for the agents [36]. A grid was built with the parameters of 42, 104 and 84 in x, y and z directions centered on this site and at a spacing of 0.458 Å. 1500 docking poses of ligands were generated and the hydrogen bonding or hydrophobic interactions of the best poses with the Aβ fibrils were analyzed by using AutoDock Tools 1.5.6. The figures were generated by using PyMol 1.8.x software.

Conflicts of interest

There are no conflicts to declare.

Acknowledgments

This work was supported by China Science Foundation (grant no. 21672043).

References

[1] R. M. Barron, D. King, M. Jeffrey, G. McGovern, S. Agarwal, A. C. Gill, P. Piccardo, PrP aggregation can be seeded by pre-formed recombinant PrP amyloid fibrils without the replication of infectious prions, *Acta Neuropathol*. 132 (2016), 611–24.

[2] M. Jucker, L. C. Walker, Pathogenic protein seeding in Alzheimer disease and other neurodegenerative disorders, *Ann Neurol.* 70 (2011), 532–40.

[3] A. Tiiman, P. Palumaa and V. Tougu, The missing link in the amyloid cascade of Alzheimer's disease-metal ions, *Neurochem. Int.* (2013) 62, 367–378.

[4] G. Bitan, M. D. Kirkitadze, A. Lomakin, S. S. Vollers, G. B. Benedek, D.B. Teplow, Amyloid beta-protein (Abeta) assembly: Abeta 40 and Abeta 42 oligomerize through distinct pathways, *Proc. Natl. Acad. Sci. USA,* (2003) 100, 330–335.

[5] Y. Eric, E. Y. Hayden, D. B. Teplow, Amyloid β-protein oligomers and Alzheimer's disease, *Alzheimers Res. Ther.* (2013) 5, 60–71.

[6] J. P. Cleary, D. M. Walsh, J. J. Hofmeister, G. M. Shankar, M. A. Kuskowski, D. J. Selkoe, K. H. Ashe, Natural oligomers of the amyloid-beta protein specifically disrupt cognitive function, *Nat. Neurosci.* (2005) 8, 79–84..

[7] J. Brouillette, The Effects of Soluble Aβ Oligomers on Neurodegeneration in Alzheimer's Disease, *Curr. Pharm. Des*. (2014) 20, 2506–2519.

[8] M. J. Rowan, I. Klyubin, Q. Wang, N. W. Hu, R. Synaptic memory mechanisms: Alzheimer's disease amyloid beta-peptide-induced dysfunction, Anwyl, *Biochem. Soc. Trans*. (2007) 35, 1219–1223.

[9] N. W. Hu, I. M. Smith, D. M. Walsh, M. J. Rowan, Soluble amyloid-beta peptides potently disrupt hippocampal synaptic plasticity in the absence of cerebrovascular dysfunction in vivo, *Brain J. Neurol*. (2008) 131, 2414–2424.

[10] P. H. Reddy, M. F. Beal, Amyloid beta, mitochondrial dysfunction and synaptic damage: implications for cognitive decline in aging and Alzheimer's disease, *Trends Mol. Med*. (2008) 14, 45–53.

[11] L. Ruan, Z. Kang, G. Pei, Y. Le, Amyloid deposition and inflammation in APPswe/PS1dE9 mouse model of Alzheimer's disease, *Curr. Alzheimer Res*. (2009) 6, 531–540.

[12] A. Salminen, J. Ojala, A. Kauppinen, K. Kaarniranta, T. Suuronen, Inflammation in Alzheimer's disease: amyloid-beta oligomers trigger innate immunity defence via pattern recognition receptors, *Prog. Neurobiol*. (2009) 87, 181–194.

[13] B. Uttara, A. V. Singh, P. Zamboni, R. Mahajan, Oxidative Stress and Neurodegenerative Diseases: A Review of Upstream and Downstream Antioxidant Therapeutic Options, *Curr. Neuropharmacol.* (2009) 7, 65–74.

[14] M. Jin, N. Shepardson, T. Yang, G. Chen, D. Walsh, D. J. Selkoe, D. J. Soluble amyloid beta-protein dimers isolated from Alzheimer cortex directly induce Tau hyperphosphorylation and neuritic degeneration, *Proc. Natl. Acad. Sci. USA,* (2011) 108, 5819–5824.

[15] P. Mishra, S. R. Ayyannan, G. Panda, Perspectives on Inhibiting β-Amyloid Aggregation through Structure-Based Drug Design, *ChemMedChem*. (2015) **10**, 1467–1474.

[16] Q. Nie, X. Du, M. Geng, Small molecule inhibitors of amyloid β peptide aggregation as a potential therapeutic strategy for Alzheimer's disease, *Acta Pharmacol. Sin*. (2011) 32, 545–551.

[17] E. Cavedo, M. O. Habert, F. Lamari, G. Gagliardi, S. Lista, M. Teichmann, H. Bakardjian, H. Hampel, B. Dubois, Preclinical Alzheimer's disease: A systematic review of the cohorts underlying the concept, *Alzheimers Dement,* (2017) 13, 454–467.

[18] M. L. Bolognesi, in Medicinal Chemistry Approaches to Personalized Medicine, K. Lackey and B. D. Roth, Wiley-VCH, (2013), ch. 9.

[19] A. Sarantopoulos, N. Beziere, V. Ntziachristos, Optical and opto-acoustic interventional imaging, *Ann Biomed. Eng*. (2012) 40, 346–366.

[20] F. Gremse, D. Doleschel, S. Zafarnia, A. Babler, W. Jahnen-Dechent, T. Lammers, W. Lederle, F. Kiessling, Hybrid μCT-FMT imaging and image analysis, *J. Vis. Exp*. (2015) 4, e52770.

[21] D. Hyde, R. De Kleine, S. A. MacLaurin, E. Miller, D. H. Brooks, T. Krucker, V. Ntziachristos, Hybrid FMT–CT imaging of amyloid-β plaques in a murine Alzheimer's disease model, *NeuroImage,* (2009) 44, 1304–1311

[22] M. Staderini, M. A. Martín, M. L. Bolognesi, J. C. Menéndez, Imaging of β-amyloid plaques by near infrared fluorescent tracers: a new frontier for chemical neuroscienc, *Chem. Soc. Rev*. (2015) 44, 1807–19.

[23] X. Zhang, Y. Z. Tian, Li, X. Tian, H. Sun, H. Liu, A. Moore, C. Ran, Design and synthesis of curcumin analogues for in vivo fluorescence imaging and inhibiting copper-induced cross-

linking of amyloid beta species in Alzheimer's disease, *J. Am. Chem. Soc*. (2013) **135**, 16397–409.

[24] P. Dao, F. Ye, Y. Z. Y. Liu, Du, K. Zhang, C. Z. Dong, B. Meunier, H. Chen, Development of Phenothiazine-Based Theranostic Compounds That Act Both as Inhibitors of β-Amyloid Aggregation and as Imaging Probes for Amyloid Plaques in Alzheimer's Disease, *ACS Chem. Neurosci*. (2017) 8, 798–806.

[25] L. Lannfelt, K. Blennow, H. Zetterberg, S. Batsman, D. Ames, J. Harrison, C. L. Masters, S. Targum, A. I. Bush, R. Murdoch, J. Wilson, C. W. Ritchie, Safety, efficacy, and biomarker findings of PBT2 in targeting Abeta as a modifying therapy for Alzheimer's disease: a phase IIa, double-blind, randomised, placebo-controlled trial, *Lancet Neurol*. (2008) 7, 779–86.

[26] A. R. White, K. J. Barnham, A. I. Bush, Metal homeostasis in Alzheimer's disease, *Expert Rev. Neurother*. (2006) 6, 711–22.

[27] N. Nguyen, A. Robert, A. L. Sournia-Saquet Vendier, B. Meunier, Characterization of new specific copper chelators as potential drugs for the treatment of Alzheimer's disease, *Chem. Eur. J.* (2014) 20, 6771–6785.

[28] X. Hu, S. L. Crick, G. Bu, C. Frieden, R. V. Pappu, J. M. Lee, Amyloid seeds formed by cellular uptake, concentration, and aggregation of the amyloid-beta peptide, *Proc. Natl. Acad. Sci. USA,* (2009) 106, 20324–20329.

[29] K. J. Barnham, C. L. Masters, A.I. Bush, Neurodegenerative diseases and oxidative stress, *Nat. Rev. Drug Discov*. (2004) 3, 205–14.

[30] T. K. Das, M. R. Wati, K. Fatima-Shad, Oxidative Stress Gated by Fenton and Haber Weiss Reactions and Its Association With Alzheimer's Disease, *Arch. Neurosci*. (2014) 2, e20078.

[31] Y. Yang, M. Cui, X. Zhang, J. Dai, Z. Zhang, C. Lin, Y. Guo, B. Liu, Radioiodinated benzyloxybenzene derivatives: a class of flexible ligands target to beta-amyloid plaques in Alzheimer's brains, *J. Med. Chem*. (2014) 57, 6030−6042.

[32] J. Michel, J. Tirado-Rives, W. L. Jorgensen, Energetics of displacing water molecules from protein binding sites: consequences for ligand optimization, *J. Am. Chem. Soc*. (2009) 131, 15403–15411.

[33] M. Clark, R. D. Cramer III, N. V. Opdenbosch, Validation of the general purpose Tripos 5.2 force field, *J. Comput. Chem*. (1989) **10**, 982–1012.

[34] J. Gasteiger, M. Marsili, Iterative partial equalization of orbital electronegativity—a rapid access to atomic charges, *Tetrahedron,* (1979) 36, 3219–3228.

[35] M. Marsili, J. Gasteiger,π Charge Distribution from Molecular Topology and π Orbital Electronegativity, *Croatica Chemica Acta,* (1980) 53, 601–614.

[36] N. P. Cook, M. Ozbil, C. Katsampes, R. Prabhakar, A. A. Marti, Unraveling the photoluminescence response of light-switching ruthenium (II) complexes bound to amyloid-β, *J. Am. Chem. Soc*. (2013) 135, 10810–10816.

Development of novel theranostic agents for in vivo amyloid imaging and protective effects on human neuroblastoma cells

Yongliang Li, Longjia Yan, Jing Cai, Wanzheng Zhang, Li Li, Zhi-yun Du, Changzhi Dong, Bernard Meunier, Huixiong Chen

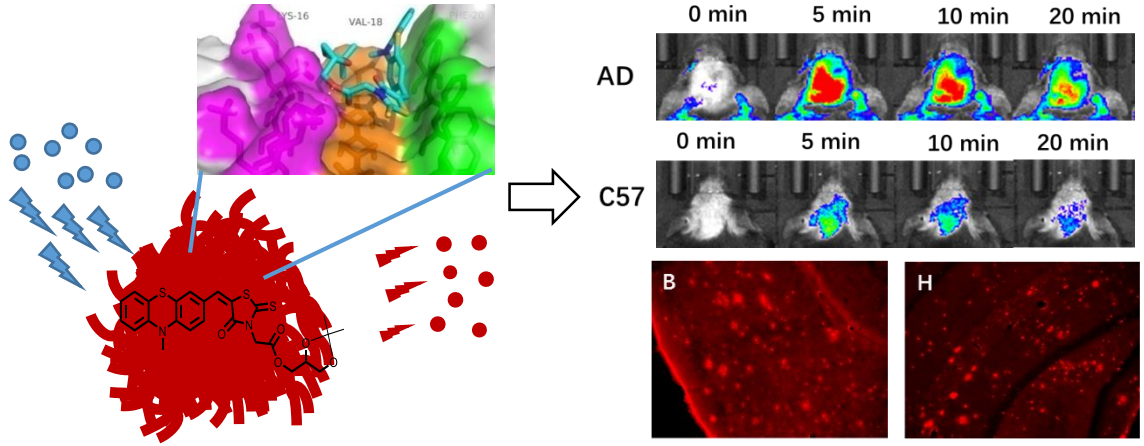

PHTZ-1: λem = 670 nm, Kd = 24.5 nM